Semiclassical motion of a multiband Bloch particle in a time-dependent field: Optical visualization

S. Longhi, M. Lobino, M. Marangoni, R. Ramponi, and P. Laporta
Dipartimento di Fisica and Istituto di Fotonica e Nanotecnologie del CNR, Politecnico di Milano, Piazza L. da Vinci 32, I-20133 Milano, Italy

E. Cianci and V. Foglietti
Istituto di Fotonica e Nanotecnologie del CNR, Sezione di Roma, Via Cineto Romano 42, 00156 Roma, Italy
(Received 28 June 2006; published 18 October 2006)

An optical visualization of the semiclassical dynamics of a multiband Bloch particle subjected to an external time-dependent force is experimentally reported using an array of tunneling-coupled lithium-niobate optical waveguides with a curved axis. It is shown that a Gaussian beam injected into the array breaks into wave packets belonging to different bands of the array which propagate as semiclassical Bloch particles in a time-dependent force simulated by the waveguide axis curvature. According to the semiclassical analysis and to numerical simulations of the scalar beam propagation equation, the paths followed by the wave packets is proven to depend on the initial momentum, which is controlled by varying the incidence angle of the Gaussian beam. In particular, we study in detail, both theoretically and experimentally, the wave packet refocusing dynamics which occurs in the presence of a semicycle sinusoidal force and reveal its deep difference with respect to Bloch oscillations in a dc field.

DOI: 10.1103/PhysRevB.74.155116 PACS number(s): 72.10.Bg, 72.90.+y, 42.82.Et

I. INTRODUCTION

The dynamics of a quantum particle in a periodic potential under the action of an external force, such as the motion of electrons in crystals induced by an applied electric field,[1] has provided since the pioneering studies by Bloch and Zener[2,3] a subject of major relevance in different physical systems. The early quantum theory of electrical conductivity in crystal lattices by Bloch and Zener led to the striking prediction that a homogeneous static electric field induces an oscillatory rather than uniform motion of the electrons, known as Bloch oscillations (BO). From the theoretical point of view, BO have been a matter of great controversy for decades, mainly related to the rigorous proof of the existence of a discrete ladder energy spectrum, that was settled only recently (for a review see, e.g., Ref. 4). From the experimental side, BO have never been observed in natural crystals because the scattering time of the electrons by the lattice defects is much shorter than the Bloch period. The first observation of BO and related Wannier-Stark ladder energy spectrum was possible using semiconductor superlattices,[5,6] where the larger spatial period leads to a much shorter Bloch period (for a review on BO in semiconductor superlattices see, e.g., Ref. 7 and references therein). In addition to semiconductor superlattices, more recently the BO motion and the existence of Wannier-Stark ladders have been theoretically studied and experimentally observed in other physical systems, including cold atoms and Bose-Einstein condensates in optical lattices,[8–11] optical waveguide arrays,[12–19] optical superlattices, and related periodic optical structures.[20–27] Other phenomena closely related to BO dynamics have been also studied and demonstrated in these systems. Among others effects, we just mention interband coupling and Zener tunneling induced by strong fields[9,17,28–31] and dynamic localization in the presence of ac or mixed ac-dc fields.[32–43]

As compared to other physical and optical systems, besides avoiding detrimental dephasing effects due to the high coherence of photons, optical waveguide arrays provide a rather unique laboratory for a visual observation of the Bloch motion in real (direct) space.[17] In addition, different launching beam geometries can be employed for band excitation control, allowing single-band[14,15,17] or multiband[44–47] excitation of the array or even the selective excitation of a single Bloch Floquet state.[44] The recent visualizations of optical Bloch wave packet motion in these structures[14,15,17,19] have considered the case of a constant transverse index gradient, which simulates the effect of a dc field in the corresponding quantum-mechanical problem, with single-band excitation at the input plane. However, as shown in Refs. 42 and 48, curved waveguides with a nonconstant curvature are suited to study wave packet dynamics under the action of a generic time-dependent force, whose strength is related to the local waveguide axis curvature by a Newtonian equation of motion.[49] For instance, we recently reported a direct experimental demonstration of the basic dynamic localization condition of electrons in a crystal subjected to an external ac force, as originally predicted by Dunlap and Kenkre,[32] by measurements of the impulse response of sinusoidally curved arrays under single band excitation.[43] Waveguide arrays with a suitably tailored axis bending thus offer the rather unique possibility to visualize in real space the semiclassical motion of Bloch wave packets in different bands under the action of any desired nonconstant force, a possibility which is hardly accessible in experiments based on condensed-matter (e.g., semiconductor superlattices) or other optical or matter-wave systems. In this work we provide a detailed theoretical and experimental study of multiband wave packet dynamics in curved waveguide arrays which mimics the semiclassical motion of a quantum particle in a periodic potential subjected to a time-dependent field. In particular, we provide a direct visualization in real space of the motion of a Bloch particle in the semicycle of a sinusoidal force, tracing the semiclassical paths of the Bloch particle in the two lowest-order bands of the array and comparing the experimental

results with the theoretical predictions. The dependence of the semiclassical Bloch path on the initial transverse photon momentum is investigated and compared to the dc force case.

The paper is organized as follows. In Sec. II the basic theoretical model describing the dynamics of an optical Bloch wave packet in a curved waveguide array, including multiband effects, is presented and applied to the array geometry used in our experiments. In Sec. III the experimental results on multiband Bloch motion of light beams in a sinusoidally curved lithium-niobate waveguide array are presented, including a visualization of the semiclassical paths for the two lowest-order bands of the array and their dependence on initial momentum. Finally, in Sec. IV the main conclusions are outlined.

II. DYNAMICS OF BLOCH WAVE PACKETS IN CURVED WAVEGUIDE ARRAYS: THEORETICAL ANALYSIS

A. Basic model and multiband excitation geometry

We consider propagation of a monochromatic wave at wavelength (in vacuum) $\lambda=2\pi/k$ in a linear array of single-mode tunneling-coupled optical waveguides, with equal separation a in the X direction, lying in the (X,Z) plane. The axis of the waveguide array is assumed to be bent along the propagation direction Z, with a paraxial bending profile $X_0(z)$ which is assumed to vary slowly over a distance of the order of the waveguide spacing a. Assuming that the field is strongly localized in the vertical Y direction, an effective two-dimensional equation can be used to study field propagation in the (X,Z) plane.[42,46,47] In the paraxial and scalar approximations, the wave equation reads (see, e.g., Refs. 42 and 49)

$$i\lambda\frac{\partial\psi}{\partial Z}=-\frac{\lambda^2}{2n_s}\frac{\partial^2\psi}{\partial X^2}+V[X-X_0(Z)]\psi, \tag{1}$$

where $\lambda\equiv\lambda/(2\pi)=1/k$ is the reduced wavelength, $V(X)\equiv[n_s^2-n^2(X)]/(2n_s)\simeq n_s-n(X)$, $n(X)$ is the effective index profile of the array in the transverse X direction, and n_s is the substrate refractive index. As noted in Ref. 49, with the formal substitution $Z\to t$, $\lambda\to\hbar$, and $n_s\to m$, Eq. (1) is analogous to the semiclassical Schrödinger equation, written in the Kramers-Henneberger reference frame,[50] for a one-dimensional electron in the periodic potential $V(X)$, subjected to an external uniform and time-dependent electric field. The oscillating term $X_0(Z)$, describing axis bending, represents the quiver motion, in the laboratory frame, of a classical electron subjected to the external field.[50] Indeed, in the waveguide reference frame:

$$x=X-X_0(Z),\quad z=Z, \tag{2}$$

and after the gauge transformation:

$$\phi(x,z)=\psi(x,z)\exp\left[-i\frac{n_s}{\lambda}\dot{X}_0(z)x-i\frac{n_s}{2\lambda}\int_0^z d\xi\dot{X}_0^2(\xi)\right] \tag{3}$$

(where the dot denotes the derivative with respect to z), Eq. (1) yields

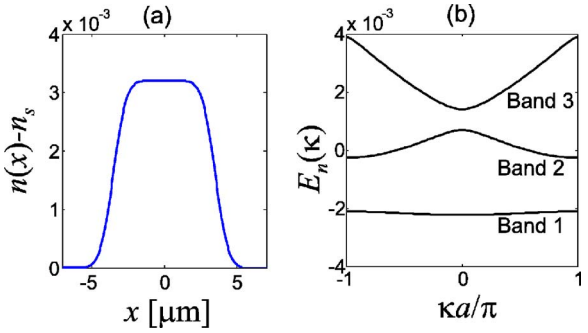

FIG. 1. (Color online) (a) Effective index profile in one period, and (b) corresponding band diagram of a waveguide array for parameter values which apply to our experiments: $a=14$ μm, $n_s=2.414$, $\lambda=1.44$ μm. In (a), the refractive index is shown in one period ($|x|<a/2$) and the profile is approximated by the function $n(x)=n_s+\Delta n[\mathrm{erf}((x+w)/D_x)-\mathrm{erf}((x-w)/D_x)]/[2\,\mathrm{erf}(w/D_x)]$, where $\Delta n=0.0032$ is the peak index change, $D_x=1$ μm is the diffusion constant, and $2w=7$ μm is the channel width.

$$i\lambda\frac{\partial\phi}{\partial z}=-\frac{\lambda^2}{2n_s}\frac{\partial^2\phi}{\partial x^2}+V(x)\phi-q\mathcal{E}(z)x\phi, \tag{4}$$

where we have set

$$q\mathcal{E}(z)\equiv-n_s\ddot{X}_0(z). \tag{5}$$

In its present form Eq. (4) is the Schrödinger equation describing the dynamics of a charged particle, of mass n_s and charge q, in a periodic potential $V[V(x+a)=V(x)]$ under the action of an applied time-dependent electric field $\mathcal{E}(z)$, whose amplitude is proportional—according to Eq. (5)—to the local curvature $\ddot{X}_0$ of the waveguide axis. Note that, in the optical analogy, the temporal variable of the quantum problem is mapped into the spatial propagation coordinate z, so that the temporal wave packet evolution of the quantum problem is visualized as paraxial propagation of light along the array.

Beam propagation in the straight array, i.e., in the absence of the external $\mathcal{E}$ field, is fully characterized by the knowledge of its band structure. Indicating by $\mathcal{H}_0=-(\lambda^2/2n_s)\partial^2/\partial x^2+V(x)$ the Hamiltonian of Eq. (4) in the absence of the external $\mathcal{E}$ field, the eigenfunctions $\phi_n(x,\kappa)$ of $\mathcal{H}_0$ are given by the Bloch-Floquet states $\phi_n(x,\kappa)=u_n(x,\kappa)\exp(i\kappa x)$ with $\mathcal{H}_0\phi_n(x,\kappa)=E_n(\kappa)\phi_n(x,\kappa)$, where n is the band index, $-\pi/a<\kappa<\pi/a$, and $E_n(\kappa)$ is the energy dispersion relation for band n. The Bloch functions satisfy the orthonormal relation $\int_{-\infty}^{\infty}dx\phi_l^*(x,\kappa')\phi_n(x,\kappa)\equiv\langle\phi_l(x,\kappa')|\phi_n(x,\kappa)\rangle=\delta_{n,l}\delta(\kappa-\kappa')$. This implies for the periodic functions $u_n(x,\kappa)$ the normalization condition $\int_{-a/2}^{a/2}dx|u_n(x,\kappa)|^2=a/(2\pi)$ and, for its Fourier coefficients $\theta_l(\kappa,n)$ defined by the relation $u_n(x,\kappa)=\sum_{l=-\infty}^{\infty}\theta_l(\kappa,n)\exp(2\pi ilx/a)$, the normalization condition $\sum_{l=-\infty}^{\infty}|\theta_l(\kappa,n)|^2=1/(2\pi)$. Figures 1(a) and 1(b) show the index profile and corresponding band diagram of a waveguide array for parameter values which apply to the structure fabricated for our experiments and described in the next section. Owing to the completeness of $\phi_n(x,\kappa)$, the field $\phi(x,z)$ can be expanded as a superposition of Bloch modes in the vari-

ous bands, i.e., one can employ the crystal momentum representation for the wave packet $\phi(x,z)$

$$\phi(x,z) = \sum_n \int_{-\pi/a}^{\pi/a} d\kappa c_n(\kappa,z) u_n(x,\kappa) \exp(i\kappa x), \qquad (6)$$

where, in the absence of the external $\mathcal{E}$ field, the coefficients c_n evolve according to $c_n(\kappa,z)=c_n(\kappa,0)\exp[-iE_n(\kappa)z/\lambda]$. The values of the coefficients c_n at the input plane $z=0$ of the array depend on the excitation beam geometry. An interesting feature of waveguide arrays, which makes them particularly suited to study wave packet dynamics, is the feasibility of the excitation geometry, which can lead to different and controllable initial conditions.[44] For instance, a single Bloch-Floquet mode for a given band can be excited using a transverse excitation geometry, where a beam is coupled at a grazing angle to the array from a region of a planar waveguide along its side,[44] whereas for broad beam incidence at the input facet of the array a superposition of Bloch modes around a given momentum κ_0, defined by the input beam angle, is excited.[44,46] In this case, multiple bands may be simultaneously excited; in particular, for a non-normal incidence at an angle corresponding to a transverse momentum close to $\kappa_0=\pi/a$, the first two bands of the array may be simultaneously excited with comparable amplitude.[46] In this work we consider the latter excitation geometry, which allows the creation of a wave packet formed by the superposition of Bloch modes belonging to different bands. For a given incident beam profile $\phi(x,0)$, the Bloch-wave spectrum $c_n(\kappa,0)$ is given by

$$c_n(\kappa,0) = \int_{-\infty}^{\infty} dx \phi_n^*(x,\kappa)\phi(x,0) \qquad (7)$$

and it can be related to the Fourier spectrum of the input beam profile, $\tilde{\phi}(\kappa)=(2\pi)^{-1/2}\int_{-\infty}^{\infty}dx\phi(x,0)\exp(-i\kappa x)$, by a simple relation. In fact, let us define the Bloch-wave excitation coefficients $B(\kappa,n)$ of the various bands, with $-\infty<\kappa<\infty$, as

$$B(\kappa,n) = \sqrt{2\pi}\theta_l^*(\kappa - 2\pi l/a, n) \qquad (8)$$

for $-\pi/a+2\pi l/a<\kappa<\pi/a+2\pi l/a$ $(l=0,\pm1,\pm2,\ldots)$. The Bloch-wave excitation coefficients $B(\kappa,n)$ are continuous functions of κ and satisfy the condition $\Sigma_n|B(\kappa,n)|^2=1$ for any κ. Thus one can easily show that (see also Ref. 46)

$$c_n(\kappa,0) = \sum_{l=-\infty}^{\infty} B(\kappa+2\pi l/a,n)\tilde{\phi}(\kappa+2\pi l/a). \qquad (9)$$

For a broad beam incident onto the array at a paraxial angle α [Fig. 2(a)], the spectrum $\tilde{\phi}(\kappa)$ is narrow around $\kappa=\kappa_0 \simeq \alpha/\lambda$, and therefore solely the Bloch modes with momentum $\kappa\simeq\kappa_0$ are mostly excited. Figure 2(b) shows the numerically computed behavior of the Bloch-wave excitation coefficients $B(\kappa,n)$ for the few low-order bands of the array depicted in Fig. 1, together with the spectrum corresponding to a typical Gaussian beam excitation used in our experiments. Note that, for a beam incidence angle α close to the Bragg angle $\alpha_B=\pi\lambda/a$, corresponding to $\kappa_0=\pi/a$, the two lowest-order bands $n=1$ and $n=2$ are almost equally excited, whereas the contributions of higher-order bands are negligible.

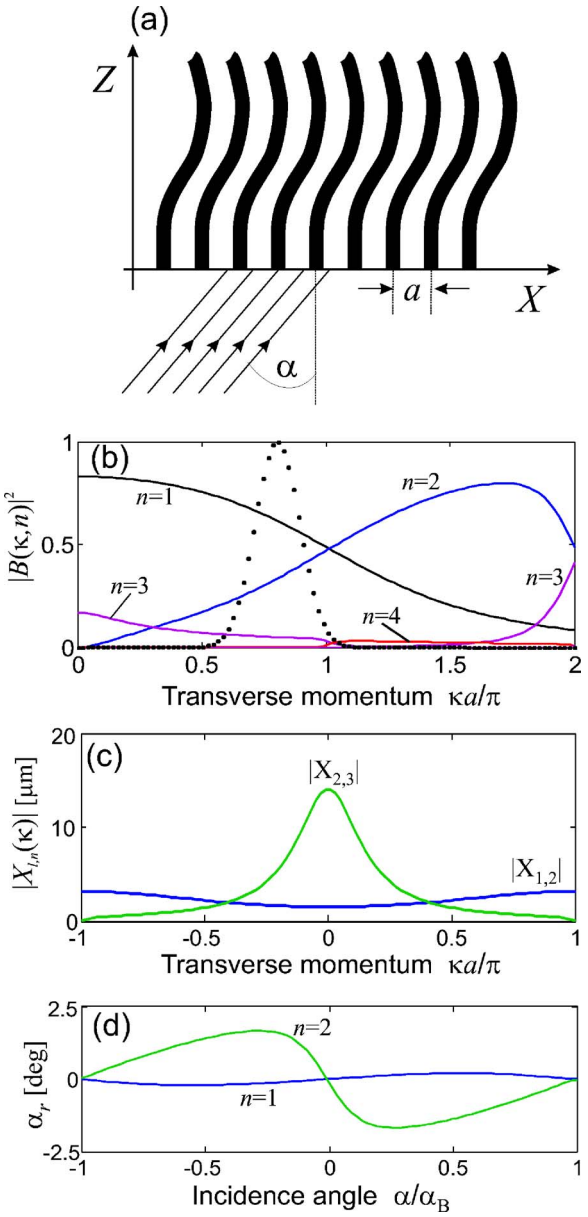

FIG. 2. (Color online) (a) Geometry for multiband array excitation. A spatially broad beam with Gaussian intensity distribution is injected into the input facet of the array at an angle α. The excited Bloch-Floquet modes in the array have a transverse momentum κ close to $\kappa_0\simeq\alpha/\lambda$. (b) Behavior of Bloch-wave excitation coefficients $|B(\kappa,n)|^2$ vs normalized transverse momentum $\kappa a/\pi$ for the four lowest-order bands of the array of Fig. 1. The dotted curve in the figure is the spectrum $|\tilde{\phi}(\kappa)|^2$ of a broad Gaussian beam with radius beam spot size $w_0=50$ μm at an incidence angle $\alpha<\alpha_B$. (c) Behavior of the interband coupling coefficients $|X_{1,2}|$ and $|X_{2,3}|$. (d) Behavior of refraction angle $\alpha_r=(1/\lambda)(dE_n/d\kappa)$ vs incidence angle α, normalized to the Bragg angle $\alpha_B=\pi\lambda/a\simeq2.95°$, for the two lowest order bands of the array.

B. Multiband wave packet dynamics in the external field

The dynamics of a Bloch wave packet in the presence of an external field has been widely discussed in the literature, especially in the presence of a dc field in connection with the well-known Bloch oscillation motion (see, for instance, Refs. 51 and 52). Here we briefly present some theoretical and general aspects of the dynamics which are of relevance for the understanding of the experimental results reported in the next section. In the crystal momentum representation [Eq. (6)], in the presence of the external $\mathcal{E}$ field the evolution equations for the coefficients $c_n(\kappa,z)$ read[51]

$$i\lambda\frac{\partial c_n}{\partial z} = E_n(\kappa)c_n - iq\mathcal{E}(z)\frac{\partial c_n}{\partial \kappa} - q\mathcal{E}(z)\sum_{l=-\infty}^{\infty} X_{n,l}(\kappa)c_l \quad (10)$$

where we have set

$$X_{n,l}(\kappa) = \frac{2\pi i}{a}\int_0^a dx\, u_n^*(x,\kappa)\frac{\partial u_l(x,\kappa)}{\partial \kappa}. \quad (11)$$

The diagonal elements $X_{n,n}$ in Eq. (10) account for the energy band correction induced by the external field, whereas the off-diagonal elements $X_{n,l}(n\neq l)$ are responsible for interband transitions (Zener tunneling). For a symmetric index profile of the waveguide, such as that considered in our experiments [see Fig. 1(a)], the periodic part of Bloch functions $u_n(x,\kappa)$ can be chosen such that $X_{n,n}=0$, whereas for $n\neq l$, $X_{n,l}$ is purely imaginary and given by (see, for instance, Ref. 53)

$$X_{n,l} = \frac{4\pi\lambda^2}{2an_s}\frac{\int_0^a dx\, u_n^*(x,\kappa)(dV/dx)u_l(x,\kappa)}{[E_n(\kappa)-E_l(\kappa)]^2}. \quad (12)$$

The numerically computed behavior of the coupling coefficients $X_{1,2}$ and $X_{2,3}$ for the lowest-order bands is shown in Fig. 2(c). We note that Zener tunneling between bands n and l may be neglected for field amplitudes such that $|q\mathcal{E}X_{n,l}|$ is smaller than the gap separation of the two bands, a requirement which is well-satisfied in our experimental conditions where solely the first two bands are populated and the band gaps are relatively wide. Under these assumptions, Eq. (10) is decoupled and can be solved in a closed form, yielding for each band:

$$c_n(\kappa,z) = g_n\left(\kappa - \frac{1}{\lambda}\int_0^z d\xi\, q\mathcal{E}(\xi)\right)\exp[-i\varphi_n(\kappa,z)], \quad (13)$$

where the spectrum $g_n(\kappa)\equiv c_n(\kappa,0)$ is determined by the input beam profile according to Eq. (9) and

$$\varphi_n(\kappa,z) = \frac{1}{\lambda}\int_0^z d\xi\, E_n\left(\kappa - \frac{1}{\lambda}\int_\xi^z d\rho\, q\mathcal{E}(\rho)\right). \quad (14)$$

Note that, according to the "acceleration theorem,"[51] the initial excitation $|g_n(\kappa)|^2$ moves along the Brillouin zone preserving its shape, namely $|c_n(\kappa,z)|^2=|g_n[\kappa-\tilde{\kappa}(z)]|^2$, where

$$\tilde{\kappa}(z) = \frac{1}{\lambda}\int_0^z d\xi\, q\mathcal{E}(\xi). \quad (15)$$

Note also that the motion of $|c_n|^2$ in the κ space is uniform solely for a constant field, i.e., in the case where the curvature of the waveguides is constant along the propagation direction. To understand the corresponding motion of the wave packet in the real space, we decompose the initial field as a superposition of wave packets belonging to different bands, i.e., we write $\phi(x,z)=\Sigma_n\psi_n(x,z)$, with $\psi_n(x,z)=\int d\kappa c_n(\kappa,z)u_n(x,\kappa)\exp(i\kappa x)$. From Eq. (13), the evolution of each wave packet is ruled by the equation

$$\psi_n(x,z) = \int d\kappa\, g_n[\kappa-\tilde{\kappa}(z)]u_n(x,\kappa)\exp[i\kappa x - i\varphi_n(\kappa,z)]. \quad (16)$$

For broad beam excitation at an incidence angle α, as discussed at the end of Sec. II A, the spectrum $g(\kappa)$ is narrow around $\kappa\sim\kappa_0=\alpha/\lambda$. Assuming that the variation of $u_n(x,\kappa)$ with κ is much smaller than that of $g_n(\kappa)$, after setting $\Delta\kappa=\kappa-\tilde{\kappa}(z)-\kappa_0$ one can write

$$\psi_n(x,z) = u_n(x,\langle\kappa\rangle)F_n(x,z)\exp[i\langle\kappa\rangle x - i\varphi_n(\langle\kappa\rangle,z)], \quad (17)$$

where the mean value of crystal momentum $\langle\kappa\rangle$ and the envelope F are given by

$$\langle\kappa\rangle = \kappa_0 + \tilde{\kappa}(z) = \kappa_0 + \frac{1}{\lambda}\int_0^z d\xi\, q\mathcal{E}(\xi), \quad (18)$$

$$F_n(x,z) = \int d\Delta\kappa g_n(\kappa_0+\Delta k)\exp[i\Delta\kappa x - i\varphi_n(\langle\kappa\rangle+\Delta\kappa,z) + i\varphi_n(\langle\kappa\rangle,z)]. \quad (19)$$

If we expand the phase term of Eq. (19) in series of $\Delta\kappa$ and limit the expansion up to first order, we obtain

$$F_n(x,z) \simeq F_n[x-x_n(z),0], \quad (20)$$

where

$$x_n(z) = \frac{1}{\lambda}\int_0^z d\xi\frac{\partial E_n}{\partial\kappa}[\kappa_0+\tilde{\kappa}(\xi)]. \quad (21)$$

Note that, according to Eqs. (17) and (20), apart from a phase term the wave packet $\psi_n(x,z)$ is given by the product of the Bloch function ϕ_n with crystal momentum $\langle\kappa\rangle=\kappa_0+\tilde{\kappa}(z)$ spanning the Brillouin zone and an envelope F which, at leading order, propagates undistorted following the trajectory $x_n(z)$ given by Eq. (21). Note that the wave packet trajectory can be obtained by solving the following semiclassical equations,[1] which directly follow from Eqs. (18) and (21):

$$\frac{d\langle k\rangle}{dz} = \frac{q\mathcal{E}(z)}{\lambda}, \quad (22)$$

$$\frac{dx_n}{dz} = \frac{1}{\chi}\frac{\partial E_n}{\partial \kappa}(\langle \kappa \rangle), \tag{23}$$

with the initial conditions $\langle \kappa \rangle(0)=\kappa_0$ and $x_n(0)=0$. Owing to the different dispersion curves of the various bands, the trajectories of the different wave packets $\psi_n(x,z)$ are distinct, which results in breakup of the overall wave packet (see, e.g., Ref. 52). In the absence of the external field, beam breakup corresponds to different refraction angles associated with the various bands of the array, i.e., different values of $(\partial E_n/\partial \kappa)_{\kappa_0}$, which depend on the incident angle as experimentally demonstrated in Refs. 44, 46, and 47. Figure 2(d) shows the numerically computed refraction angles $\alpha_r \simeq (1/\chi)(dE_n/d\kappa)$ of the wave packets for different bands vs the incidence angle α for the straight array. Note the characteristic periodicity of refraction angles vs α and the existence of negative refraction.

C. Semiclassical motion and beam refocusing in a constant force and in a semicycle sinusoidal force

The paths followed by the wave packets ψ_n, excited at the input plane of the array, are ruled by the semiclassical equations (22) and (23) and are thus determined by both band dispersion curves and external force. Under certain conditions the wave packets, after initial breakup due to different refraction angles, may refocus at the same plane or may even reconstruct their initial shape, apart from a global phase that depends on band order. Since refocusing at a plane z simply implies $x_n(z)=x_n(0)=0$ for each wave packet and initial κ_0 value, the condition for full wave reconstruction in each band is more stringent and, neglecting interband interactions (Zener tunneling), it requires that $\tilde{\kappa}(z)$ be an integer multiple of $2\pi/a$ [Eq. (15)] and $\varphi_n(\kappa,z)$ [Eq. (14)] be independent of κ. These conditions, which follow from Eqs. (13)–(15), are rigorously met for a dc field $\mathcal{E}=\mathcal{E}_0$, for which a reconstruction of the wave packets ψ_n for the various bands is periodically attained at distances multiples of the Bloch period $z_B=2\pi\chi/(q\mathcal{E}_0 a)$ (Bloch oscillations). Such a reconstruction is related to the existence of a Wannier-Stark ladder for the energy spectrum of the Hamiltonian $\mathcal{H}_0 - q\mathcal{E}_0 x$ in the single-band approximation.[4] For single band excitation, such periodic motion has been previously visualized in waveguide arrays with a constant transverse index gradient.[14,15,17] In case of multiband excitation and neglecting Zener tunneling, for a constant force the initial wave packet breaks up and the paths of the different band wave packets ψ_n in the real space follow the corresponding band profile in the reciprocal space, namely from Eqs. (22) and (23) one easily obtains

$$x_n(z) = \frac{1}{q\mathcal{E}_0}[E_n(\kappa_0 + q\mathcal{E}_0 z/\chi) - E_n(\kappa_0)] \tag{24}$$

and

$$\langle \kappa \rangle = \kappa_0 + q\mathcal{E}_0 z/\chi. \tag{25}$$

After one Bloch period, i.e., at $z=z_B$, the wave packets ψ_n thus refocus at the same initial position. As briefly reviewed in the Appendix, the refocusing for a dc force actually corresponds to exact field reconstruction for each band wave packet (in the limit of negligible Zener tunneling).

A second important case of wave packet refocusing is the multiband motion of a Bloch particle in a sinusoidal ac field, which is obtained in our optical system using a periodic waveguide curvature $X_0(z)=A\sin(2\pi z/\Lambda)$, leading to the time-dependent force [see Eq. (5)]

$$q\mathcal{E}(z) = \frac{4\pi^2 n_s A}{\Lambda^2}\sin\left(\frac{2\pi z}{\Lambda}\right), \tag{26}$$

where A and Λ are the amplitude and period of axis bending, respectively. The corresponding motion in the reciprocal space of the mean value of wave packet momentum $\langle \kappa \rangle$ is thus [see Eq. (18)]

$$\langle k \rangle = \kappa_0 + \frac{\Gamma}{a}\left[1 - \cos\left(\frac{2\pi z}{\Lambda}\right)\right], \tag{27}$$

where we have set

$$\Gamma = \frac{4\pi^2 n_s a A}{\lambda \Lambda}. \tag{28}$$

We note that the motion of a Bloch particle in a sinusoidal ac field has been widely studied in the context of dynamic localization,[32,33,36,38] a phenomenon of periodic self-imaging of the wave packet, which follows the ac field and which is analogous to BO. For a sinusoidal ac field, periodic field reconstruction in a given band strictly requires a band profile of sinusoidal shape,[38] and therefore it is only approximate; this point is reviewed for the sake of clearness in the Appendix. The condition for dynamic localization in a sinusoidal ac field is[32] $J_0(\Gamma)=0$, which has been experimentally verified in our recent work by studying the impulse response of sinusoidally curved arrays.[43] Here we aim to study the semiclassical motion of a broad beam under multiband excitation conditions and intend to visualize the Bloch motion in one semicycle of the sinusoidal force. From the point of view of the center-of-mass wave packet motion, the semicycle time-dependent force bears a close connection to BO because, after propagation for a half period (i.e., for $z=\Lambda/2$), the wave packets excited in the different bands refocus at the same position whenever the dynamic localization condition $J_0(\Gamma)=0$ is satisfied. In fact, by approximating the band profile $E_n(\kappa)$ with a sinusoidal curve, $E_n(\kappa)=E_n(0)+\Delta_n[1-\cos(\kappa a)]$, from Eq. (21) one has

$$\begin{aligned} x_n(z) &= -\frac{a\Delta_n}{\chi}\,\mathrm{Im}\left\{\exp[-i(\kappa_0 a + \Gamma)] \times \int_0^z d\xi \exp[i\Gamma\cos(2\pi\xi/\Lambda)]\right\} \\ &= \frac{a\Delta_n J_0(\Gamma) z}{\chi}\sin(\kappa_0 a + \Gamma) + \frac{a\Delta_n \Lambda}{\lambda}\sum_{l\neq 0}\frac{J_l(\Gamma)}{l} \\ &\quad \times\{\sin[\kappa_0 a + \Gamma - (l-1)\pi/2 - 2\pi z l/\Lambda] \\ &\quad - \sin[\kappa_0 a + \Gamma - (l-1)\pi/2]\}. \end{aligned} \tag{29}$$

Hence for $z=\Lambda/2$ and when the dynamic localization condition $J_0(\Gamma)=0$ is satisfied, one has $x_n(\Lambda/2)=x_n(0)=0$. It should be noted that beam path convergence at $z=\Lambda/2$ is independent of both the initial momentum κ_0 (i.e., incidence angle) and band order n provided that the approximation of a sinusoidal band profile is valid. Such an approximation is reasonable for the first two bands of the array shown in Fig. 1, which are the ones excited in our experiments. In practice, as it will be shown in both simulations and experimental results discussed in the next section, the incident beam first breaks up into two wave packets, belonging to the two first bands of the array, which follow different trajectories according to Eq. (21) but finally they recombine and return to its initial position. This refocusing behavior, though being similar to the one previously discussed for BO in a dc field, does not correspond to wave packet reconstruction, as shown in the Appendix. This remarkable difference as compared to BO in a dc field is related to the fact that in the semicycle sinusoidal field the final momentum $\langle k\rangle$ does not return to its initial value κ_0 [compare Eqs. (25) and (27)]. Therefore even within the single-band and sinusoidal-band-shape approximations, exact field reconstruction is not achieved in the semicycle sinusoidal field. A simple and experimentally accessible demonstration of such a different behavior is provided by a measure of wave packet displacement $\Delta x=|x_2-x_1|$ vs κ_0 (i.e., incidence angle) in the middle plane between the input and focusing planes. For a dc field, at $z=z_B/2$ the crystal momentum $\langle\kappa\rangle$ spans half of the full Brillouin zone [from the initial value κ_0 to the final value $\kappa_0+\pi/a$, see Eq. (25)], and the corresponding beam displacement is obtained from Eq. (24) and reads

$$\Delta x=\frac{1}{q\mathcal{E}_0}|E_2(\kappa_0+\pi/a)-E_1(\kappa_0+\pi/a)+E_1(\kappa_0)-E_2(\kappa_0)|. \tag{30}$$

Note that Δx turns out to be a symmetric function around $\kappa_0=\pi/a$, with a maximum displacement at $\kappa_0=\pi/a$, i.e., for an incidence angle $\alpha=\alpha_B$. For instance, if we approximate the first two bands of the array by sinusoidal curves, $E_{1,2}(\kappa)=E_{1,2}(0)+\Delta_{1,2}[1-\cos(\kappa a)]$ with $\Delta_1>0$ and $\Delta_2<0$, one has

$$\Delta x=\frac{2az_B}{\lambda}|\Delta_2-\Delta_1||\cos(\kappa_0 a)|. \tag{31}$$

Conversely, for the sinusoidal field, the crystal momentum $\langle\kappa\rangle$ at $z=\Lambda/4$ spans less than half of the full Brillouin zone [from the initial value κ_0 to the final value $\kappa_0+\Gamma/a$ with $\Gamma\simeq 2.405$, corresponding to the first zero of the Bessel J_0 function; see Eq. (27)]. From Eq. (29), the beam displacement under the approximation of sinusoidal band profiles can be then calculated yielding:

$$\Delta x=\frac{2a\Lambda\sigma}{\lambda}|\Delta_2-\Delta_1||\cos(\kappa_0 a+\Gamma)| \tag{32}$$

with $\sigma=\Sigma_{n=0}^{\infty}J_{2n+1}(\Gamma)/(2n+1)\simeq 0.589$. In deriving Eq. (32), we approximated as in Eq. (31) the profiles of the first two bands by sinusoidal curves. As opposed to Eq. (31), for the sinusoidal field the beam displacement Δx is not symmetric around $\kappa_0=\pi/a$, i.e., around the Bragg angle α_B, which is just related to the fact that in the reciprocal space the crystal momentum spans less than half of the Brillouin zone. In the experiment discussed in the next section this feature will be evidenced by the asymmetry around the Bragg angle α_B of the measured beam displacement Δx vs incidence angle α (see Fig. 8 discussed in Sec. III B).

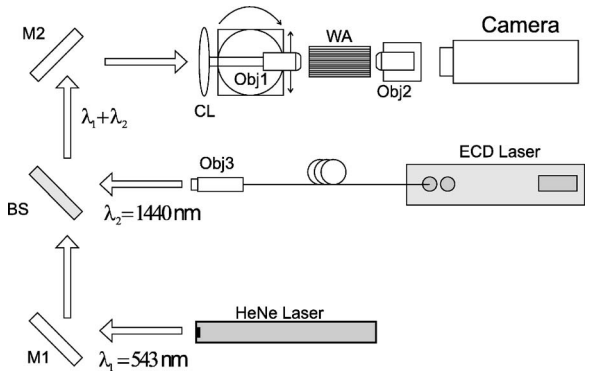

FIG. 3. Schematic of the experimental setup. Obj: microscope objective; BS: beam splitter; M: mirror; CL: cylindrical lens; ECD: external cavity diode; and WA: waveguide array.

III. EXPERIMENTAL RESULTS

To experimentally study the semiclassical Bloch motion under the action of a time-dependent field, we manufactured a set of waveguide arrays in z-cut lithium niobate substrates using the annealing proton exchange (APE) technique.[54] Each array is composed by 80 waveguides with $2w=7$ μm channel width and $a=14$ μm spacing, which are single-mode at the working wavelength of $\lambda=1.44$ μm. The waveguide arrays were patterned by deposing a titanium mask on a lithium niobate substrate, and they were fabricated by 57 min proton exchange at 247 °C in a melt of benzoic acid with 1% lithium benzoate and 4 h 55 min annealing at 350 °C in air. The sample is $L=28$-mm long and comprises a straight array, which allows us to experimentally characterize its band structure in the absence of external field, and a curved array in which the axis bending is shaped according to $X_0(z)=A\sin(2\pi Z/\Lambda)$, with $A\simeq 164$ μm and $\Lambda=56$ mm. The curved array thus simulates the action of a half-cycle of an ac sinusoidal field, and the design parameters of the array are chosen such that the dynamic localization condition $\Gamma\simeq 2.405$ is attained at the probing wavelength $\lambda=1.44$ μm [see Eq. (28)]. Figure 3 shows the experimental setup used for coupling light into the arrays at different incident angles and for monitoring and recording the intensity patterns at the output facet. The arrays were illuminated by an external cavity diode (ECD) laser tuned at $\lambda=1.44$ μm, whose output is collimated and superimposed to an He-Ne laser beam at $\lambda=543$ nm used for alignment purposes. The radiation is coupled into the waveguides through a cylindrical telescope formed by a cylindrical lens of 140 mm focal length and a spherical objective with 10 mm focal length, producing an elliptical beam waist diameter of 100 μm in the horizontal x

direction and 8 μm in the vertical y direction. The telescope is mounted on a translational-rotational stage which permits one to change the angle of incidence with an accuracy of 0.01° and to change the beam incident point by translating the telescope in the x direction with a 1 μm accuracy. The polarization of the incident beam was set orthogonal to the plane of the waveguides in order to couple the TM modes supported by the APE waveguides. The intensity profile at the output facet of the array is then imaged and recorded on a vidicon camera by a 10× collecting objective. In order to visualize the Bloch motion along the propagation direction, three other identical curved arrays with the same design parameters were fabricated and cut at different lengths L=7, 14, and 21 mm, which allow us to monitor the light intensity distribution at planes $\Lambda/8$, $\Lambda/4$, and $3\Lambda/8$, respectively, of the semicycle sinusoidal force.

A. Multiband beam dynamics in the straight array

In order to check the quality of the fabricated sample and to demonstrate multiband excitation and beam breakup due to different refraction angles, we first studied beam propagation in the straight array. We note that similar measurements demonstrating multiband effects were previously reported for a straight array of ridge waveguides etched onto an AlGaAs substrate,[44] however, the semiclassical Bloch motion in curved arrays, simulating the action of the time-dependent force, was not investigated. Figure 4(a) shows, as an example, the measured transverse intensity profile at the output plane of the L=28-mm-long array when it is illuminated, at the input plane, by a Gaussian beam (radius spot size $w_0 \simeq 50$ μm) tilted at an angle $\alpha \simeq 3.51°$. The position x=0 corresponds, in the figure, to the input waveguide at which the Gaussian beam was centered. Figure 4(b) shows the corresponding theoretical prediction based on a direct numerical analysis of Eq. (4). The measure clearly indicates beam breakup due to the simultaneous excitation of the first two bands of the array, according to Fig. 2(b). The beam ψ_1, corresponding to the first band, has a negative refraction angle, and hence at the output it is shifted on the left side, whereas the beam ψ_2, corresponding to the excitation of band 2, has a positive refraction angle and at the output it is shifted at positive values of x. The refraction angles corresponding to the measure of Fig. 4(a) turn out to be in very good agreement with those obtained from band analysis [Fig. 2(d)]. The two images in Fig. 4(a) show two particulars of the measured transverse light spots, taken in correspondence of the centers of the two beams ψ_1 and ψ_2, together with the position of the waveguides in the array. Note that, while for beam ψ_1 the light is mostly confined in the waveguides, for the second beam ψ_2 the light is mainly confined in the low-index regions, i.e., outside the waveguides. This behavior reflects the shapes of the Bloch-Floquet modes of the first two bands of the array, which are depicted in Fig. 4(c): as the Bloch modes in band 1 confine the field in the high-index region of the array, for the Bloch modes belonging to band 2 the opposite behavior occurs. Figure 5 shows, for the straight array, a sequence of recorded output intensity distributions as a function of the input beam angle α. Excitation of the two

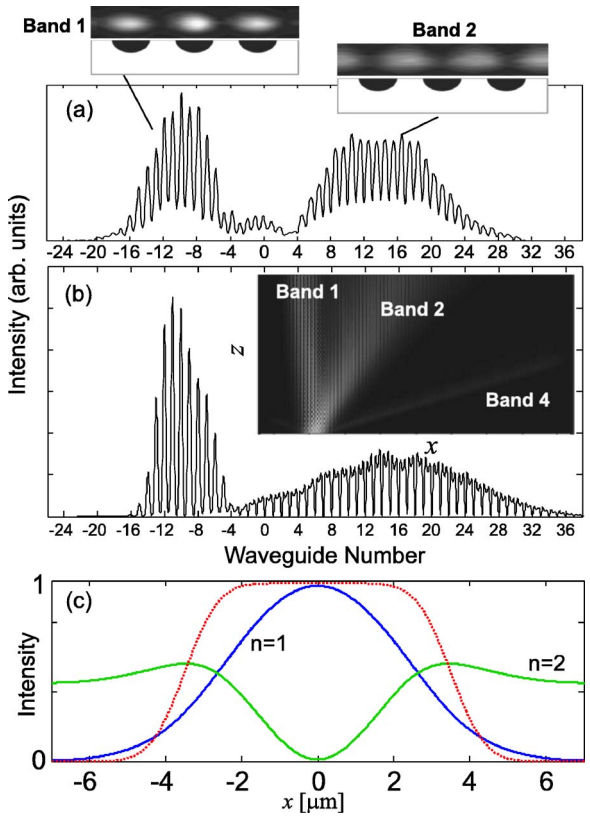

FIG. 4. (Color online) (a) Horizontal cross section of measured light intensity profile at the output plane of the L=28-mm-long straight array illuminated by a w_0=50 μm-spot-size Gaussian beam at an incidence angle α=3.51° ($\alpha/\alpha_B \simeq 1.2$). The two insets show particulars of the two-dimensional transverse images recorded on the camera taken in correspondence of the centers of the two splitted beams belonging to the first two bands of the array. The position of the channel waveguides with respect to the light spots are also schematically depicted at the bottom of each image. (b) Intensity field distribution at the output plane of the array as predicted by a numerical analysis of Eq. (4). The inset shows the wave packet breakup dynamics along the propagation distance (top view) as obtained by the numerical simulations. Note that, in addition to bands 1 and 2, a weak excitation of band 4 is also visible. (c) Numerically computed intensity profiles of Bloch-Floquet modes at κ=0.8 $\times \pi/a$ for the first two bands of the array. The dotted curve shows, for comparison, the refractive index profile in one period.

bands is clearly visible, with an intensity of the beam belonging to band 2 which increases as the incident angle is increased and becomes dominant as the Bragg angle α_B is crossed, in agreement with the theoretical analysis shown in Fig. 2(b). The transverse lateral shifts of the splitted wave packets also turn out to be in good quantitative agreement with the numerically computed refraction angles shown in Fig. 2(d).

B. Bloch motion in the semicycle curved array

A series of detailed measurements on beam dynamics in the semicycle curved array vs the incidence angle α, i.e., initial wave packet momentum κ_0, have been performed and compared to the theoretical predictions based on the semi-

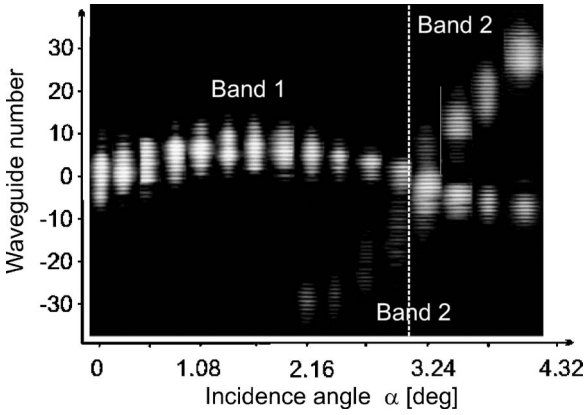

FIG. 5. Measured light intensity distributions at the output plane of the 28-mm-long straight array vs incidence angle. The array is illuminated by a $w_0=50$ μm-spot-size Gaussian beam. The vertical dashed line corresponds to beam incidence at the Bragg angle $\alpha=\alpha_B\simeq 2.95°$.

classical results of Sec. II C and on direct numerical simulations of Eq. (4). For a given incidence angle close to the Bragg angle, the input Gaussian beam breaks up mainly into two wave packets of comparable amplitude, belonging to the first two bands of the array, as for the straight array case discussed in Sec. III A. However, in the curved array the applied field changes the momentum in the reciprocal space according to Eq. (27), and correspondingly the center of mass of the two beams follow again two distinct but *curved* trajectories that are obtained by solving Eq. (23). These trajectories strongly depend on the initial beam momentum κ_0. For instance, if the dispersion curves of the two bands are approximated by sinusoidal curves, the beam paths are given by Eq. (29). The dependence of the beam trajectories on the initial momentum is demonstrated in Fig. 6, where the beam evolution obtained by numerical simulations of Eq. (4) and the corresponding measured transverse intensity light distributions at the five plane $z=0$, $z=7$ mm, $z=14$ mm, $z=21$ mm, and $z=28$ mm are shown for two different values of the incidence angle. For the sake of readability, the measured light intensity distributions are represented in the waveguide reference frame $x=X-X_0(z)$, where the waveguides appear to be straight. Note that the beams belonging to the first two bands of the array clearly follow different paths for the two incidence angles, however, they refocus at the output plane and recombine in a single beam according to the semiclassical analysis (see Sec. II C): in fact, for $\Gamma\simeq 2.405$ and approximating the band dispersion profile by a sinusoidal curve, according to Eq. (29) one has $x_n(\Lambda/2)=0$ independently of the incidence angle. Note also that Zener tunneling of the two wave packets, which would correspond to beam breakup at the turning points of the beam trajectory where the wave packet momentum reaches the minimum of band-gap separation, is negligible. This result is in good agreement with energy band and Zener coefficient calculations shown in Fig. 2: in fact, for the design parameters of the curved array the maximum amplitude of the applied force during the semicycle is $4\pi^2 n_s A/\Lambda^2 \simeq 4.42$ m^{-1} [see Eq. (26)], and therefore from Fig. 2(c) we

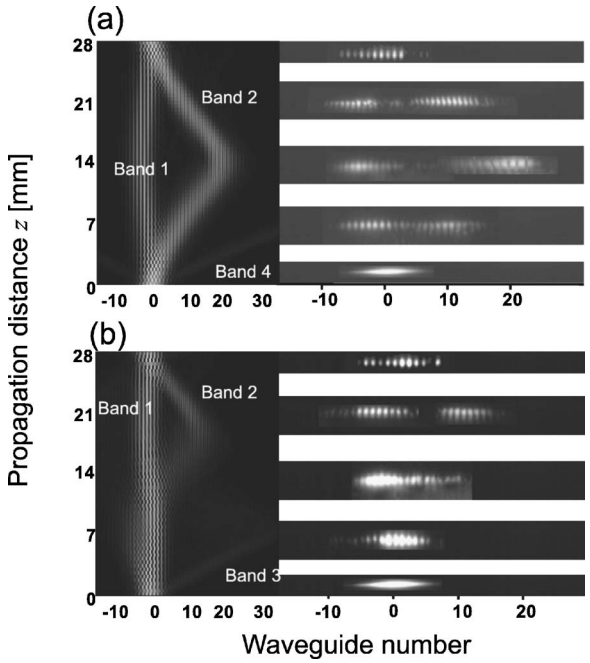

FIG. 6. Bloch wave-packet dynamics in a semicycle sinusoidal field for two different incidence angles. (a) $\alpha/\alpha_B=1.2$, and (b) $\alpha/\alpha_B=0.8$. The right images show the measured transverse light distribution at different propagation lengths [from bottom to the top: $z=0$ (input beam), $z=7$ mm, $z=14$ mm, $z=21$ mm, and $z=28$ mm (output beam)]. The left plots show the detailed beam dynamics as predicted by a direct numerical analysis of Eq. (4). For the sake of readability, both theoretical and experimental data are represented in the waveguide reference frame $x=X-X_0(Z)$ and $z=Z$.

can estimate $|q\mathcal{E}X_{1,2}|\simeq 1.41\times 10^{-5}$ and $|q\mathcal{E}X_{2,3}|\simeq 6.23\times 10^{-5}$, which should be compared with the band-gap separation $E_g\simeq 1.84\times 10^{-3}$ and $E_g\simeq 7.27\times 10^{-4}$ between the corresponding bands. Since $E_g \gg |q\mathcal{E}X|$, Zener tunneling is negligible from band 1 to band 2, and from band 2 to band 3. In the numerical simulations of Fig. 6 excitation of small-amplitude wave packets belonging to higher-order bands is also visible, however, these wave packets tunnel into higher-order bands and are not visible in our experimental measurements.

The independence of beam refocusing of incidence angle at the output plane of the semicycle array is clearly demonstrated in Fig. 7, where a sequence of recorded output intensity distributions are shown for a few values of the input beam angle α. Note that, contrary to the straight array measurements (Fig. 5) where beam breakup was clearly visible at the output plane at any incidence angle $\alpha\neq\alpha_B$, in the present case the refocusing of the two beams belonging to the first two bands of the array is attained at the output plane for any incidence angle. Beam refocusing dynamics and recombination at the output plane of the semicycle curved array as shown in Fig. 6 closely resembles the dynamics of a two-band Bloch oscillator in one Bloch period: the initial wave packet first breaks up into two wave packets belonging to the first two bands of the array, which follow different paths but finally recombine after one Bloch period z_B. However, we stress that, as in the dc field case a field reconstruction of each wave packet occurs after one Bloch period, this is not

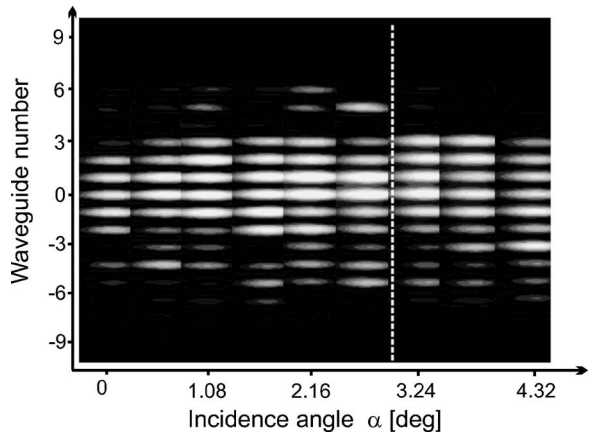

FIG. 7. Same as Fig. 5, but for the semicycle curved array.

the case of the semicycle sinusoidal field, as shown in Sec. II C and in the Appendix. In fact, for the semicycle sinusoidal field the final mean-value $\langle\kappa\rangle$ of wave packet momentum does not return to its initial value κ_0 and, according to Eq. (13), wave packets reconstruction in each band is not achieved, despite the wave packets refocus at the same position $x_n=0$ at $z=\Lambda/2$. As shown in Sec. II C, the failure of wave packet momentum return can be visualized at best by measuring the lateral shift $\Delta x=|x_2(\Lambda/4)-x_1(\Lambda/4)|$ of the two wave packets at the middle plane between input ($z=0$) and refocusing ($z=\Lambda/2$) planes. In fact, as for a Bloch oscillator in a dc field such a lateral shift turns out to be a symmetric function of incidence angle α around the Bragg angle α_B [see Eqs. (30) and (31)], for the semicycle sinusoidal field the symmetry is broken due to nonreturn of the wave packet momentum [see Eq. (32)]. We experimentally demonstrated the asymmetry of the lateral shift Δx by measuring the output light distribution vs the incidence angle in the sample cut at $z=\Lambda/4=14$ mm. The experimental results are shown in Fig. 8(a) and compared to the theoretical predictions based on the semiclassical analysis [Fig. 8(b)]. Note that the behavior of measured lateral shift Δx of the two beams belonging to the two bands of the array is in good agreement with the theoretical calculation.

IV. CONCLUSIONS

In this work we studied both theoretically and experimentally the semiclassical motion of a Bloch particle subjected to an external time-dependent force and provided a direct visualization of the wave packet dynamics by using an array of curved optical waveguides, in which the waveguide curvature is tailored to simulate the action of a semicycle sinusoidal force. In particular, we considered an operational regime where the first two energy bands are simultaneously excited but Zener tunneling is negligible. Beam breakup due to multiband excitation and beam refocusing were observed in agreement with the semiclassical analysis. We also presented a detailed analysis of beam path dependence on initial momentum and demonstrated the distinct features of beam refocusing observed in the semicycle time-dependent field as

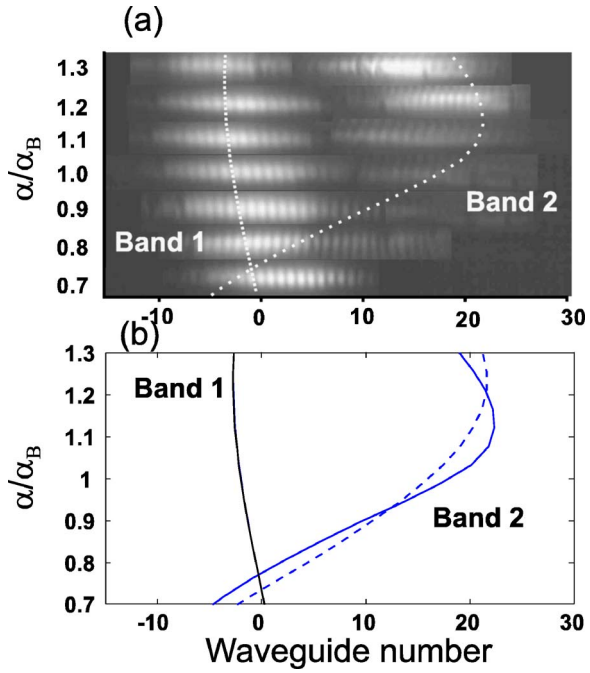

FIG. 8. (Color online) (a) Measured intensity light distributions at the exit of the quarter-cycle curved array ($z=14$ mm) for a few values of incidence angle α normalized to the Bragg angle α_B. The input field is a Gaussian beam with radius spot size $w_0\simeq 50$ μm. The dashed curves are the beam center of mass positions predicted by the semiclassical analysis. (b) Transverse beam shift (in units of waveguide separation) vs incidence angle for the wave packets in the first two bands of the array as predicted by a numerical integration of Eqs. (22) and (23) (solid curves) and by assuming a sinusoidal shape for the energy bands [dashed curves; see Eq. (32)]. For band 1, the solid and dashed curves are almost overlapped.

compared to the usual Bloch oscillations induced by a dc force.

ACKNOWLEDGMENTS

This research was partially funded by MIUR (FIRB project). The authors acknowledge A. Minotti, S. Quaresima, and M. Scarparo for their technical assistance.

APPENDIX

In this Appendix we briefly review the conditions for wave packet reconstruction in the single-band approximation. For a dc field $\mathcal{E}(z)=\mathcal{E}_0$, wave reconstruction is achieved at propagation distances multiple of the Bloch period $z_B=2\pi\lambda/(aq\mathcal{E}_0)$. In fact, at $z=z_B$ from Eqs. (14) and (15) one has $\tilde{k}=2\pi/a$ and $\varphi_n(\kappa,z_B)=z_B\bar{E}_n/\lambda$, where $\bar{E}_n=(a/2\pi)\int_{-\pi/a}^{\pi/a}d\kappa E_n(\kappa)$ is the dc term in the Fourier expansion of the energy dispersion curve $E_n(\kappa)$. Therefore from Eq. (13) it follows that $c_n(\kappa,z_B)=c_n(\kappa,0)\exp[-iz_B\bar{E}_n/\lambda]$ and hence $\psi_n(x,z_B)=\psi_n(x,0)\exp[-iz_B\bar{E}_n/\lambda]$.

For an ac field, the problem of field reconstruction is more involved and related to dynamic localization (for more details we refer to Refs. 32, 36, 38, and 39). For an ac field of

period Λ, at $z=\Lambda$ one has $\tilde{\kappa}=0$ [see Eq. (15)], whereas the phase $\varphi_n(\kappa,\Lambda)$ can be calculated from Eq. (14) by writing the energy dispersion curve $E_n(\kappa)$, which is periodic in κ with period $2\pi/a$, as a Fourier series $E_n(\kappa)=\Sigma_l \epsilon_l \exp(i\kappa a)$. One obtains

$$\varphi_n(\kappa,\Lambda)=\frac{1}{\chi}\sum_{l=-\infty}^{\infty}\epsilon_l \exp[il\kappa a]\int_0^{\Lambda} d\xi \exp[il\gamma(\xi)], \quad \text{(A1)}$$

where we have set

$$\gamma(\xi)\equiv\frac{a}{\chi}\int_0^{\xi} d\rho q\mathcal{E}(\rho). \quad \text{(A2)}$$

In the single-band approximation, the condition for wave reconstruction is that $\varphi_n(\kappa,\Lambda)$ be independent of κ. From Eq. (A1) it follows that, for an ac field, wave reconstruction is attained provided that

$$\int_0^{\Lambda} d\xi \exp[il\gamma(\xi)]=0 \quad \text{(A3)}$$

for any $l=\pm 1,\pm 2,\ldots$. We note that the condition expressed by Eq. (A3) for dynamic localization under the single-band approximation was previously derived in Ref. 38 using a Wannier function basis for the wave packet. As shown in Refs. 38 and 39, Eq. (A3) can be simultaneously met only for ac fields that are discontinuous at all changes of sign. However, if the band curve $E_n(\kappa)$ has a sinusoidal shape, i.e., the Fourier coefficients ϵ_l vanish for $|l|\geqslant 2$, dynamic localization simply requires

$$\int_0^{\Lambda} d\xi \exp[i\gamma(\xi)]=0. \quad \text{(A4)}$$

For example, in a sinusoidal ac field, $\mathcal{E}(z)=\mathcal{E}_0\sin(2\pi z/\Lambda)$, Eq. (1) leads to the well-known condition $J_0(\Gamma)=0$ with $\Gamma=a\Lambda q\mathcal{E}_0/\lambda$, as originally derived by Dunlap and Kenkre.[32] We finally note that beam refocusing in a semicycle of a sinusoidal field, discussed in Sec. II C and observed in Figs. 6 and 7, does not correspond to field reconstruction for each band wave packet. In fact, at $z=\Lambda/2$ one can show, assuming a sinusoidal band shape and after some straightforward calculations, that $\varphi_n(\kappa,\Lambda/2)$ is independent of κ as for the dc field case, however, $\tilde{\kappa}(\Lambda/2)=2\Gamma/a$ does not vanish nor is it an integer multiple of $2\pi/a$, as for the dc case. This means, according to Eq. (13), that at $z=\Lambda/2$ the Bloch wave spectrum is shifted from its initial distribution and field reconstruction is not achieved.

[1] N. W. Ashcroft and N. D. Mermin, *Solid State Physics* (Saunders, Philadelphia, 1976).
[2] F. Bloch, Z. Phys. **52**, 555 (1928).
[3] C. Zener, Proc. R. Soc. London, Ser. A **145**, 523 (1934).
[4] G. Nenciu, Rev. Mod. Phys. **63**, 91 (1991).
[5] E. E. Mendez, F. Agullo-Rueda, and J. M. Hong, Phys. Rev. Lett. **60**, 2426 (1988); P. Voisin, J. Bleuse, C. Bouche, S. Gaillard, C. Alibert, and A. Regreny, *ibid.* **61**, 1639 (1988).
[6] C. Waschke, H. G. Roskos, R. Schwedler, K. Leo, H. Kurz, and K. Köhler, Phys. Rev. Lett. **70**, 3319 (1993).
[7] M. Glück, A. R. Kolovsky, and H. J. Korsch, Phys. Rep. **366**, 103 (2002).
[8] M. BenDahan, E. Peik, J. Reichel, Y. Castin, and C. Salomon, Phys. Rev. Lett. **76**, 4508 (1996).
[9] B. P. Anderson and M. A. Kasevich, Science **282**, 1686 (1998).
[10] O. Morsch, J. H. Müller, M. Cristiani, D. Ciampini, and E. Arimondo, Phys. Rev. Lett. **87**, 140402 (2001).
[11] O. Morsch and M. Oberthaler, Rev. Mod. Phys. **78**, 179 (2006).
[12] U. Peschel, T. Persch, and F. Lederer, Opt. Lett. **23**, 1701 (1998).
[13] G. Lenz, I. Talanina, and C. M. de Sterke, Phys. Rev. Lett. **83**, 963 (1999).
[14] T. Pertsch, P. Dannberg, W. Elflein, A. Bräuer, and F. Lederer, Phys. Rev. Lett. **83**, 4752 (1999).
[15] R. Morandotti, U. Peschel, J. S. Aitchison, H. S. Eisenberg, and Y. Silberberg, Phys. Rev. Lett. **83**, 4756 (1999).
[16] B. A. Usievich, V. A. Sychugov, J. Kh. Nirligareev, and K. M. Golant, Opt. Spectrosc. **97**, 841 (2004); J. Kh Nirligareev, K. M. Golant, V. A. Sychugov, and B. A. Usievich, Quantum Electron. **35**, 917 (2005).
[17] H. Trompeter, T. Pertsch, F. Lederer, D. Michaelis, U. Streppel, A. Bräuer, and U. Peschel, Phys. Rev. Lett. **96**, 023901 (2006).
[18] H. Trompeter, W. Krolikowski, D. N. Neshev, A. S. Desyatnikov, A. A. Sukhorukov, Yu. S. Kivshar, T. Pertsch, U. Peschel, and F. Lederer, Phys. Rev. Lett. **96**, 053903 (2006).
[19] N. Chiodo, G. Della Valle, R. Osellame, S. Longhi, G. Cerullo, R. Ramponi, P. Laporta, and U. Morgner, Opt. Lett. **31**, 1651 (2006).
[20] G. Monsivais, M. del Castillo-Mussot, and F. Claro, Phys. Rev. Lett. **64**, 1433 (1990).
[21] C. M. de Sterke, J. E. Sipe, and L. A. Weller-Brophy, Opt. Lett. **16**, 1141 (1991)
[22] C. M. de Sterke, J. N. Bright, P. A. Krug, and T. E. Hammon, Phys. Rev. E **57**, 2365 (1998).
[23] A. Kavokin, G. Malpuech, A. DiCarlo, P. Lugli, and F. Rossi, Phys. Rev. B **61**, 4413 (2000).
[24] G. Malpuech, A. Kavokin, G. Panzarini, and A. DiCarlo, Phys. Rev. B **63**, 035108 (2001).
[25] R. Sapienza, P. Costantino, D. Wiersma, M. Ghulinyan, C. J. Oton, and L. Pavesi, Phys. Rev. Lett. **91**, 263902 (2003).
[26] V. Agarwal, J. A. del Rio, G. Malpuech, M. Zamfirescu, A. Kavokin, D. Coquillat, D. Scalbert, M. Vladimirova, and B. Gil, Phys. Rev. Lett. **92**, 097401 (2004).
[27] V. Lousse and S. Fan, Phys. Rev. B **72**, 075119 (2005).
[28] M. Jona-Lasinio, O. Morsch, M. Cristiani, N. Malossi, J. H. Müller, E. Courtade, M. Anderlini, and E. Arimondo, Phys. Rev. Lett. **91**, 230406 (2003).
[29] B. Rosam, K. Leo, M. Glück, F. Keck, H. J. Korsch, F. Zimmer, and K. Köhler, Phys. Rev. B **68**, 125301 (2003).
[30] M. Ghulinyan, C. J. Oton, Z. Gaburro, L. Pavesi, C. Toninelli, and D. S. Wiersma, Phys. Rev. Lett. **94**, 127401 (2005).

[31] A. Fratalocchi and G. Assanto, Opt. Lett. **31**, 1489 (2006).
[32] D. H. Dunlap and V. M. Kenkre, Phys. Rev. B **34**, 3625 (1986).
[33] M. Holthaus, Phys. Rev. Lett. **69**, 351 (1992).
[34] X.-G. Zhao, R. Jahnke, and Q. Niu, Phys. Lett. A **202**, 297 (1995).
[35] B. J. Keay, S. Zeuner, S. J. Allen, K. D. Maranowski, A. C. Gossard, U. Bhattacharya, and M. J. W. Rodwell, Phys. Rev. Lett. **75**, 4102 (1995).
[36] M. Holthaus and D. W. Hone, Philos. Mag. B **74**, 105 (1996).
[37] K. W. Madison, M. C. Fischer, R. B. Diener, Q. Niu, and M. G. Raizen, Phys. Rev. Lett. **81**, 5093 (1998).
[38] M. M. Dignam and C. M. de Sterke, Phys. Rev. Lett. **88**, 046806 (2002).
[39] P. Domachuk, C. M. de Sterke, J. Wan, and M. M. Dignam, Phys. Rev. B **66**, 165313 (2002).
[40] G. Lenz, R. Parker, M. C. Wanke, and C. M. Sterke, Opt. Commun. **218**, 87 (2003).
[41] J. Wan, C. M. de Sterke, and M. M. Dignam, Phys. Rev. B **70**, 125311 (2004).
[42] S. Longhi, Opt. Lett. **30**, 2137 (2005).
[43] S. Longhi, M. Marangoni, M. Lobino, R. Ramponi, P. Laporta, E. Cianci, and V. Foglietti, Phys. Rev. Lett. **96**, 243901 (2006).
[44] D. Mandelik, H. S. Eisenberg, Y. Silberberg, R. Morandotti, and J. S. Aitchison, Phys. Rev. Lett. **90**, 053902 (2003).
[45] D. Mandelik, H. S. Eisenberg, Y. Silberberg, R. Morandotti, and J. S. Aitchison, Phys. Rev. Lett. **90**, 253902 (2003).
[46] A. A. Sukhorukov, D. Neshev, W. Krolikowski, and Y. S. Kivshar, Phys. Rev. Lett. **92**, 093901 (2004).
[47] R. Morandotti, D. Mandelik, Y. Silberberg, J. S. Aitchison, M. S. Demetrios, N. Christodoulides, A. A. Sukhorukov, and Y. S. Kivshar, Opt. Lett. **29**, 2890 (2004).
[48] S. Longhi, M. Marangoni, D. Janner, R. Ramponi, P. Laporta, E. Cianci, and V. Foglietti, Phys. Rev. Lett. **94**, 073002 (2005).
[49] S. Longhi, D. Janner, M. Marano, and P. Laporta, Phys. Rev. E **67**, 036601 (2003).
[50] M. Pont, N. R. Walet, M. Gavrila, and C. W. McCurdy, Phys. Rev. Lett. **61**, 939 (1988).
[51] J. Callaway, *Quantum Theory of the Solid State* (Academic Press, New York, 1974), pp. 465–478.
[52] T. Hartmann, F. Keck, H. J. Korsch, and S. Mossmann, New J. Phys. **6**, 2 (2004).
[53] V. S. Shchesnovich and S. B. Cavalcanti, J. Phys. B **39**, 1997 (2006).
[54] M. L. Bortz and M. M. Fejer, Opt. Lett. **16**, 1844 (1991).